applied optics

Excitation of surface plasmon polaritons in a gold nanoslab on ion-exchanged waveguide technology

Ricardo Tellez-Limon,[1,5] Sylvain Blaize,[2] Florent Gardillou,[3] Victor Coello,[4] and Rafael Salas-Montiel[2,*]

[1]CONACYT-Unidad Monterrey, Centro de Investigación Científica y de Educación Superior de Ensenada, Alianza Centro 504, PIIT, Apodaca, Nuevo León CP 66629, Mexico
[2]Department of Physics, Mechanics, Materials, Nanotechnologies, ICD/L2n CNRS, Université de Technologie de Troyes, 12 rue Marie Curie CS 42060, Troyes 10004, France
[3]Teem Photonics, 61 chemin du Vieux Chêne, Meylan F-38240, France
[4]Unidad Monterrey, Centro de Investigación Científica y de Educación Superior de Ensenada, Alianza Centro 504, PIIT, Apodaca, Nuevo León CP 66629, Mexico
[5]e-mail: rtellez@conacyt.mx
*Corresponding author: rafael.salas@utt.fr

Received 29 October 2019; revised 10 December 2019; accepted 11 December 2019; posted 11 December 2019 (Doc. ID 381915); published 10 January 2020

Integrated metaphotonic devices has opened new horizons to control light-guiding properties at nanoscale; particularly interesting is the application of plasmonic nanostructures coupled to dielectric waveguides to reduce the inherent light propagation losses in metallic metamaterials. In this contribution, we show the feasibility of using ion-exchanged glass waveguides (IExWg) as a platform for the efficient excitation of surface plasmon polaritons (SPP). These IExWg provide high coupling efficiency and low butt-coupling with conventional dielectric optical waveguides and fibers, overcoming the hard fabrication tunability of commonly used CMOS-guiding platforms. We present a near-field scanning optical microscopy characterization of the propagation characteristics of SPP supported in a gold nanoslab fabricated on top of an IExWg. We found that the SPP can be only be excited with the fundamental TM photonic mode of the waveguide. Thanks to the low propagation loss, low birefringence, and compatibility with optical fibers, glass waveguide technology is a promising platform for the development of integrated plasmonic devices operating at visible and near infrared wavelengths with potential applications in single molecule emission routing or biosensing devices.

https://doi.org/10.1364/AO.381915

1. INTRODUCTION

The interaction of electromagnetic waves considering both electric and magnetic fields with structured metamaterials has been largely studied in recent years, leading to a new research field called metaphotonics [1,2]. An ultimate aim is to combine different optical components into single miniature optical chips that serve as a bridge to overcome the huge size mismatch between diffraction-limited microphotonics and bandwidth-limited nanoelectronics [3,4]. These on-chip architectures provide new degrees of freedom to control light guiding at nanoscale, a key feature for the next generation of optical communications, biomedical, quantum, computational networks, and sensing technologies [5–8].

Among the large variety of integrated metaphotonic devices [9], metallic stripes surrounded by dielectric media allow light propagation through the excitation of the so-called short- and long-range surface plasmon polaritons (SPP). Different configurations for the proper excitation of these SPP modes have been proposed, but absorption in metals limits light propagation [10,11] to the micrometer scale [12] and to the millimeter scale [13]. An alternative to overcome this limitation is by integrating metallic nanostructures to dielectric waveguides, being excited hybrid photonic–plasmonic modes [14]. With this approach, several optical effects have been demonstrated, including high directionality of confined light [15] and strong light confinement of guided plasmonic modes in arrays of gold nanoparticles integrated on top of dielectric waveguides [16,17], as well as all-optical modulators [18] and integrated devices for on-chip sensing and spectroscopy applications [19,20].

Most of these integrated structures make use of complementary metal-oxide-semiconductor (CMOS) substrates, like silicon-on-insulator waveguides, limiting their operation to near-infrared wavelengths [21,22]. Although the scope of applications of integrated optical devices such as biosensing requires that these systems also operate in the VIS and near-IR, which is a benefit of operation in the first biological window [23]. To overcome this spectral limitation, lithium niobate on insulator [24] or silicon nitride on insulator [25] platforms have been employed. However, due their aspect ratio and high index contrast between the core and the surrounding media, these waveguides suffer from modal birefringence, strong nonlinear effects, hard tunability, and coupling losses [26]. Hence, it is crucial to explore new combinations of hybrid metaphotonic platforms with efficient and fast reconfigurability toward high-performing devices with engineered optical properties for state-of-the-art applications.

Glass waveguides are an alternative low-cost technology that has been barely employed for integrated plasmonics. Since they emerged in the early 1970s, these waveguides have been largely employed in telecommunications because of their compatibility with optical commercial fibers [27]. Their design principle is based on the local substitution of relatively mobile Na+ or K+ ions in glass by other ions of different size and polarizability [28]. This ionic diffusion process modifies the electronic structure of glass, yielding to a gradient variation of the refractive index in a selected region, and allowing patterning of waveguiding regions in planar substrates [29]. Some advantages of this waveguiding platform are the ease of fabrication and tunability of its optical properties, like low birefringence, burring depth, and low index contrast that produce a large evanescent field to properly excite plasmonic resonances [30–32] as well as semiconductor quantum dots emission [33]. Integration of ion exchange technology with overlaid metal and high-contrast index materials is seen as an evolution of this technology [34].

In this contribution, we demonstrate the excitation of SPPs with ion-exchanged glass waveguides (IExWg) and show the feasibility of combining these two well-known technologies as platform for the design of integrated metaphotonic devices. To this purpose, we designed an IExWg that supports only the two first nondegenerated fundamental TE0 and TM0 modes and characterized its effective index mode by near-field scanning optical microscopy (NSOM) in a heterodyne configuration. Then, we demonstrate its viability as platform for integrated metaphotonic devices by exciting the SPP resonances of a gold nanoslab placed on top of it (Fig. 1), being experimentally verified with the NSOM technique that the plasmonic resonance of the slab is only excited with the fundamental TM0 mode of the waveguide. These results give us an insight into the potential applications of the IExWg as a platform for the development of low-cost integrated optical devices operating at visible wavelengths for on-chip applications.

2. DESIGN AND FABRICATION OF THE INTEGRATED STRUCTURE

A. Ion-Exchanged Glass Waveguide

To design and model the optical properties of the IExWg, we used a theoretical model to predict the distribution of the index of refraction. This distribution is assumed to be linearly proportional to the concentration profile of the ions $C(x, y)$ involved in the ion exchange process as

$$n(x, y, \lambda) = n_{\text{sub}}(\lambda) + \Delta n_0(\lambda) C(x, y), \tag{1}$$

where $n_{\text{sub}}(\lambda)$ is the refractive index of the substrate, and $\Delta n_0(\lambda)$ is an experimental value related to the maximum increase of refractive index that can be achieved with a maximum ion concentration (i.e., $C = 1$). The index distribution is thus controlled by the concentration profile. The dynamics of the ion concentration profile is in turn governed by the diffusion Eq. (9) (in reference [35]). Using finite difference methods (FDM), we numerically solved this equation with the following parameters: 20% silver ions (Ag^+), exchange temperature $T = 603$ K, exchange time $t = 4$ min, and $\Delta n_0(\lambda) = 0.08$. The diffusion parameters were $D_{\text{Ag}} 1.3 \times 10^{-15}$ m^2/s, $\alpha = 0.9$ [36], and the ions' diffusion window ranging from 1 μm to 2 μm. The index distribution for a glass waveguide with the previous parameters and a diffusion window of 1.5 μm is depicted in Fig. 2(a).

The dispersion relation [Fig. 2(b)]. as well as the optical mode profiles [Figs. 2(c) and 2(d)]. were calculated using the FDM implemented by MODE solution Lumerical. For this purpose, we formatted our index data into the data format for importing n and k isotropic materials into MODE solutions. We then calculated the dispersion relation in a spectral range from 500 nm to 1.0 μm, and obtained two nondegenerated guided modes [Fig. 2(b)]. The traverse electric (TE) mode, with the electric field horizontally oriented, had an effective index $n_{\text{eff}} = 1.51$ at a wavelength $\lambda = 633$ nm (Fig. 2c), while the transverse magnetic TM mode, with an electric field vertically oriented, had an effective index $n_{\text{eff}} = 1.509$ at the same wavelength [Fig. 2(d)].

Following the theoretical design and numerical modeling, the IExWg was fabricated with the use of photolithography to define the diffusion window of 1.5 μm width along a 1 cm by 1 cm glass substrate. The patterned sample was submerged in a molten salt (Ag^+/Na^+, 20% Ag^+) in an oven at $T = 603$ K [31,35]. Finally, the mask was removed by wet etching.

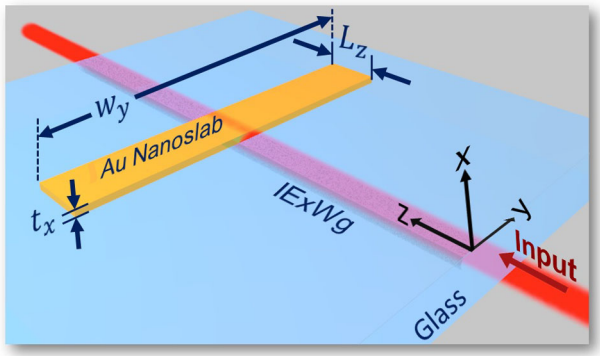

Fig. 1. Schematic representation of a gold nanoslab on top of an ion-exchanged glass waveguide. The thickness of the slab is $t_x = 30$ nm, depth is $L_z = 5.6$ μm, and width is $w_y = 50$ μm. The width of the slab can be considered as invariant in the y direction as it is much larger than the width of the IExWg ($w_{\text{IExWg}} = 1.5$ μm).

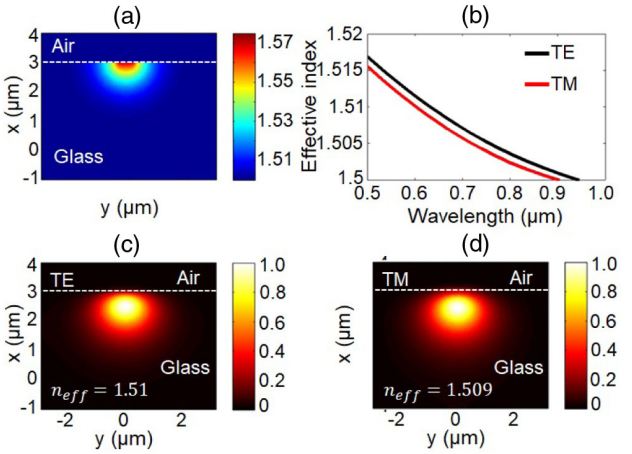

Fig. 2. Design and modeling of an ion-exchanged glass waveguide. (a) Distribution of the refractive index of an IExWg with $\Delta n_0(\lambda) = 0.08$ and a diffusion window of 1.5 μm. (b) Dispersion curves of the IExWg exhibiting two TE and TM modes in a spectral range from 0.5 to 1 μm. (c) and (d) Near-field maps of the electric field distribution for the TE and TM modes, at a wavelength $\lambda = 633$ nm, with effective indices 1.51 and 1.509, respectively.

B. Gold Nanoslab on Glass Substrate

At a single dielectric/metal interface, a SPP mode can only be excited with TM-polarized incident waves characterized by a complex wavevector for noble metals. For multilayered systems consisting of successive metal/dielectric thin films, SPPs are supported at each interface. These SPPs are coupled if the thickness of the intermediate metallic layer is shorter that their decay length [37]. By performing 1D FDTD simulations, Fig. 3 shows the dispersion curves [Fig. 3(a)] for a SPP at an air/gold/glass interface [Fig. 3(b)]. The refractive index for the metallic layer was obtained by using the dielectric function of gold fitted from experimental ellipsometry measurements and considered a refractive index for the glass substrate of $n = 1.505$.

The dispersion curves of the three-layered system [Fig. 3(a)] present two branches corresponding to the modes at the air/Au (black curve) and Au/glass interfaces (blue curve). The wavevectors of these modes, defined as $\beta = k_0 n_{\text{eff}} = (2\pi/\lambda) n_{\text{eff}}$, are $\beta_r = k_0(1.0336 + i0.0030)$ and $\beta_{nr} = k_0(1.7827 + i0.0399)$ at $\lambda = 660$ nm, respectively, and their propagation lengths, defined as $L = (2\text{Im}\{\beta\})^{-1}$, are $L_r = 17.507$ μm and $L_{nr} = 1.316$ μm. The first one is a radiative mode with effective index close to the free space light-line (black curve in Fig. 3(c), while the second one is a nonradiative mode confined in the metal surface [blue curve in Fig. 3(c)], corresponding to a SPP resonance. As it is well known, SPPs cannot be directly excited with a wavevector k_0 because of the mismatch between frequency and wavevector (i.e., $k > k_0$), situation that can be observed in the dispersion curves Fig. 3(a). Hence, it is necessary to excite them through phase-matching techniques, such as prism coupling [37], grating coupling [13,38], or near-field excitation [39] to add the extra wavevector required for their excitation.

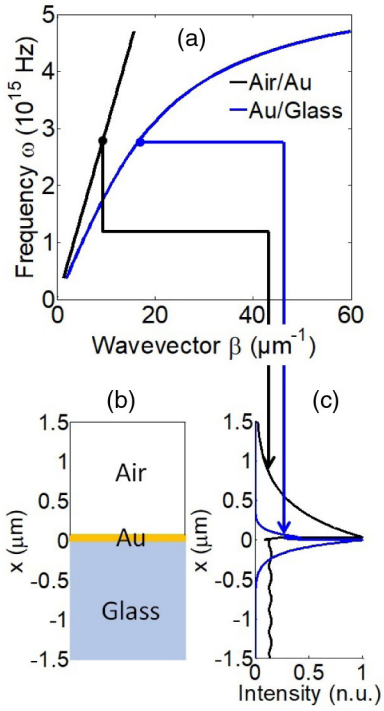

Fig. 3. Surface plasmon polariton in a three-layered system. (a) Dispersion curves of an SPP at gold/glass (blue curve) and air/gold (black curve) interfaces. (b) Schematic representation of the air/gold/glass media. (c) Intensity profiles along the x direction for the SPPs at the Air/Au (black curve) and Au/Glass (blue curve) interfaces at a wavelength $\lambda = 660$ nm.

C. Gold Nanoslab on Top of an Ion-Exchanged Glass Waveguide

Another possibility for SPP excitation and to satisfy the wavevector matching condition is making use of guided modes [17]. Hence, we designed a three-layered system consisting of air, a gold nanoslab, and an IExWg on glass (Fig. 1). As the wavevectors of the TM mode of the IExWg propagate along the metal/glass interface, they can be used to efficiently excite the SPP of the gold nanoslab. Besides, IExWg on glass provides an excellent platform as the optical modes with high butt-coupling efficiency with optical fibers. Moreover, this platform can be incorporated in current optical fiber systems.

Including the Au nanoslab on top of the IExWg in our modeling, we calculated the dispersion relation and mode profiles (Fig. 4). Besides the air light-line, the dispersion curves of the layered system air/metal nanoslab/IExWg present two branches corresponding to the odd (green curve) and even (blue curve) plasmonic modes [Fig. 4(a)]. The wavevectors of these modes are $\beta_o = k_0(1.5028 + i0.0001)$ and $\beta_e = k_0(1.8764 + i0.0282)$ at $\lambda = 660$ nm, while their propagation lengths are $L_o = 525.21$ μm and $L_e = 1.86$ μm, respectively. As can be regarded in the near-field maps of the electric field amplitude, the odd mode is mainly confined in the waveguide region [Fig. 4(b)], while the even mode is confined to the metal surface [Fig. 4(c)]. The maps of the real part of the E_x field component, show the asymmetry for the odd mode [Fig. 4(d)] and symmetry for the even mode [Fig. 4(e)]. Since both even and odd modes are coupled, this three-layered system

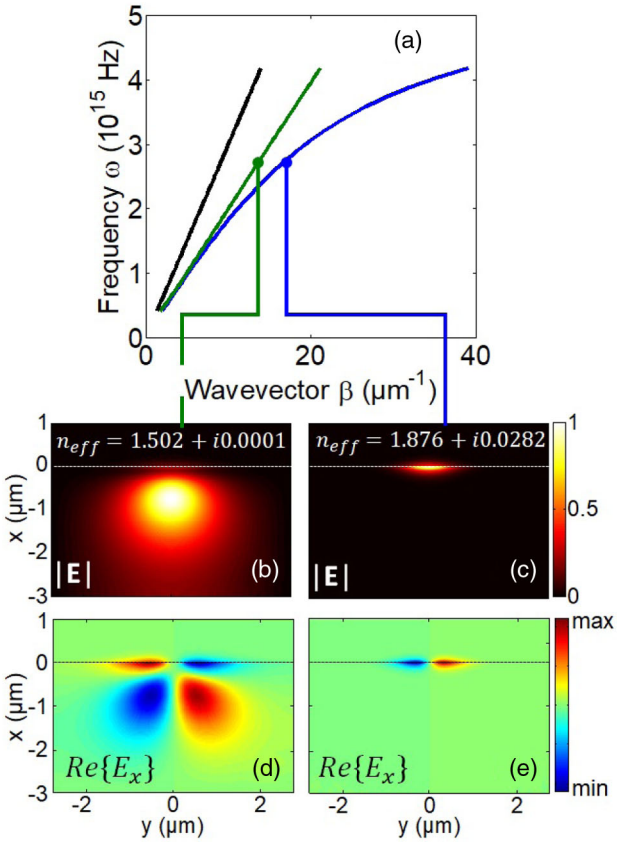

Fig. 4. Surface plasmon polariton in a gold nanoslab integrated on IExWg. (a) Dispersion curves of a gold nanoslab on top of the waveguide. Normalized near-field maps of the electric field amplitude of (b) even and (c) odd coupled modes at $\lambda = 660$ nm. The field maps in (d) and (e), correspond to the real part of the E_x field component for the odd and even modes, respectively, confirming their asymmetry.

can be regarded as a parallel two-waveguide directional coupler, being excited by the SPP through evanescent coupling with the mode of the IExWg. This mode coupling leads to vertical light beating in the coupling region [40], with a coupling length between these two waveguides, defined as $L_c = \pi/|\beta_e - \beta_o|$, is $L_c = 0.88$ μm at $\lambda = 660$ nm. By using coupling mode theory [41,42], the coupling efficiency between these two waveguides is 96.4% at the beginning of the slab (xy plane at $z = 0$ nm), and 89.7% at 500 nm from this point (xy plane at $z = 500$ nm). These values compete with Si waveguiding platforms, though without the need of tapered structures to efficiently excite SPP [43].

D. Fabrication of Gold Nanoslab on Top of An IExWg

Following the theoretical design, we fabricated a gold nanoslab on top of the IExWg. The waveguide was fabricated by Teem Photonics in an optical glass substrate with a roughness < 0.5 nm. The facets of the substrate were meticulously polished with abrasive diamond grits of different grain size to reduce their roughness to < 5 nm. For the plasmonic layer, we used electron beam lithography (EBL), metallization, and a lift-off process. The nanoslab patterning on top of the IExWg was carefully aligned during the EBL process. We used polymethyl methacrylate (PMMA) as electron beam resist, exposed with an acceleration voltage of 10 keV, had an area dose of 300 μC/cm^2, and a working distance of 8 mm. A 35 nm thickness gold layer with an average roughness of about 0.9 nm was deposited with a Joule effect evaporator, with the interposition of an 8 nm thick indium thin oxide (ITO) thin film (MEB 400, Plassys).

3. RESULTS AND DISCUSSION

First, we experimentally characterized the glass waveguides in the far field as well as in the near-field optical regimes. For the far field, we measured the transmission spectra by using a supercontinuum light source and an optical spectrum analyzer butt-coupled with optical fibers to the fabricated IExWg to determine their cut-off wavelengths. To map the near field above the surface of the waveguide, we developed a NSOM system by combining an atomic force microscope (AFM) probe with the integrated optics setup, with a He–Ne laser operating at a wavelength $\lambda = 633$ nm to illuminate the system. With this coherent light source we used interferometry in our NSOM to measure both the amplitude and phase of the local electric field [44]. With this phase map, we measured the effective index of the mode propagating through the waveguide (Fig. 5).

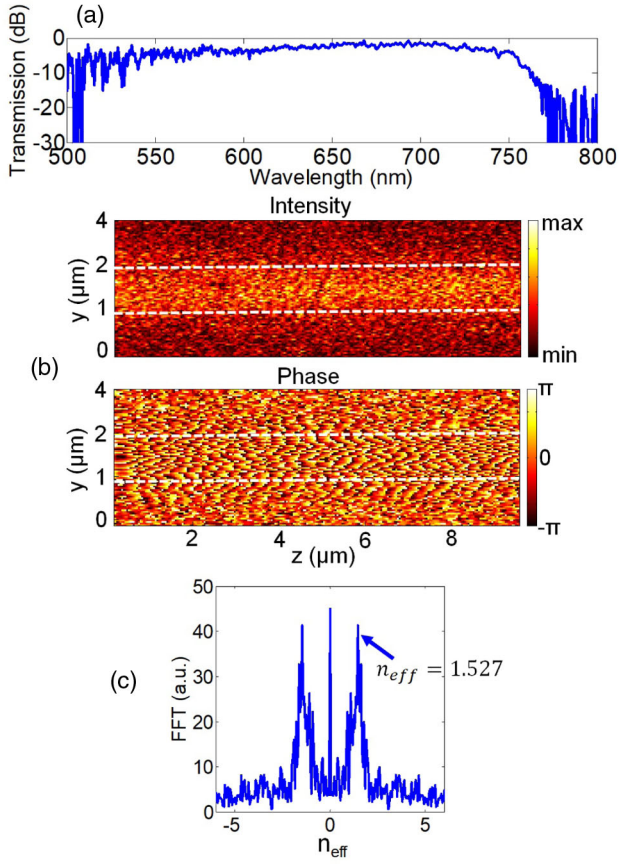

Fig. 5. Far-field and near-field optical characterization of ion-exchanged waveguide. (a) The transmission spectrum provides the cut-off wavelength of the IExWg ($\lambda_c = 780$ nm). (b) NSOM images of the intensity and phase of the local electric field above an IExWg. (c) Spatial FFT along the propagation direction of the measured electric near field.

The power transmission measured at the output of the waveguide was normalized relative to that of the light source. The transmission includes coupling losses, losses by Fresnel reflections at the air/glass interface, and propagation losses. For an IExWg with a diffusion window of 1.5 μm, the experimental cut-off wavelength was $\lambda_c = 780 \pm 50$ nm. Discrepancies between this value and theoretical predictions (Fig. 2) arises from small variations in the refractive index of the real substrate and IExWg. This value corresponds to the wavelength at which the power transmission decreases by half of the maximum power at the 30 dB level [Fig. 5(a)].

By making use of the NSOM system in a heterodyne configuration (interference with a probe beam), we obtained both intensity and phase near-field maps [Fig. 5(b)]. Using fast Fourier transform (FFT), it was possible to determine the effective index of the waveguide. For the single mode IExWg, this value was $n_{\text{eff}} = 1.527 \pm 0.17$ at a wavelength $\lambda = 633$ nm [Fig. 5(c)]. Due to the low index contrast between the substrate and the waveguide, both the amplitude and phase maps presented a low-intensity contrast in the waveguiding region, reducing the resolution for the measurement of the effective index through the FFT.

We then characterized the integrated system formed by the gold nanoslab on top of the single mode IExWg (Fig. 1). First, we measured the transmission spectrum of the integrated structure for TM polarization [Fig. 6(a)]. This spectrum was normalized to the spectrum of an IExWg without any structure. As can be observed, the optical losses (absorption, scattering, reflection) are of almost 25 dB. Then, we characterized the structure in the near field by using the NSOM technique in a transmission configuration [45–47] using a light source of wavelength $\lambda = 660$ nm butt-coupled to the integrated device with a single-mode tapered microlensed polarization maintaining optical fiber with a tip radius of around ~ 1 μm to prevent a size mismatch between the fiber and the IExWg. An intermediate pig-tailed polarization rotator was employed to properly select the horizontal (TE mode) or vertical (TM mode) polarization state. Due to the low power (5 mW) of the He–Ne laser previously used for the characterization of the IExWg, we were not able to clearly observe the near-field maps. For this reason, we used a higher power pig-tailed diode laser source operating at $\lambda = 660$ nm to clearly observe the SPP mode hybridization (beating period), as will be shown, at the expense of losing the phase measurements (heterodyne detection).

Figure 6(b) shows the topography of the sample captured with the AFM probe, as well as the intensity near-field distributions obtained with the NSOM when the gold nanoslab was excited with TE [Fig. 6(c)] and TM [Fig. 6(d)] modes of the waveguide. As can be observed, the SPP was efficiently excited when the IExWg was excited with the TM mode. This is a natural result because the width of the nanoslab is larger than the width of the waveguide; hence the nanoslab can be considered as invariant along the horizontal plane and, for this geometry, the SPP can only be excited with TM polarized light [37]. Because of the mode coupling between the TM photonic mode and the SPP, a clear spatial beating is observed [Fig. 6(d)] with a period of 1.01 ± 0.19 μm, which is close to the calculated coupling length (section 2.3). This spatial beating (lobes observed on top of the nanoslab) is characteristic of a two-waveguide hybrid

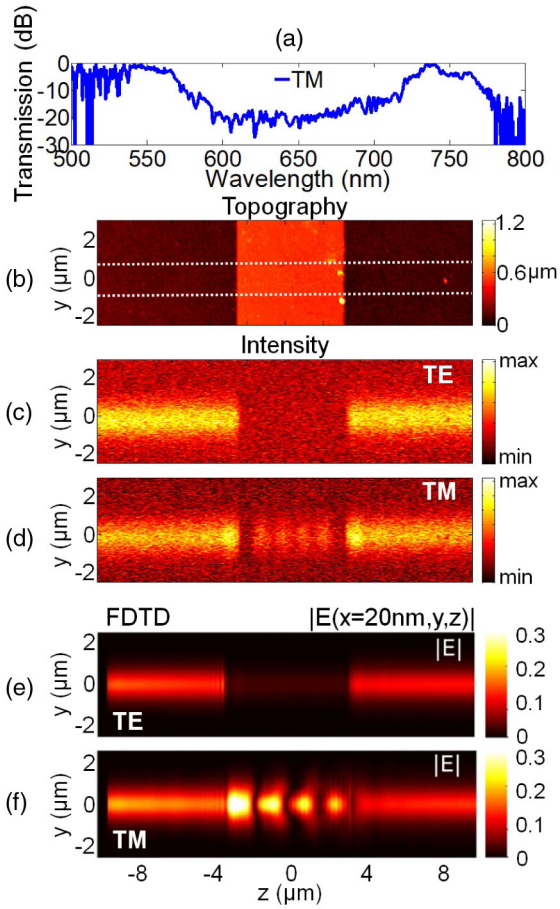

Fig. 6. Characterization of the gold nanoslab integrated to the IExWg. (a) Far-field transmission spectrum normalized to that of an isolated IExWg. (b) Topography of the gold nanoslab on top of the IExWg. The dotted lines indicate the guiding region. (c) and (d) Intensity NSOM images of the hybrid system for both TE and TM fundamental modes of the IExWg at a wavelength $\lambda = 633$ nm, respectively. (e) and (f) FDTD calculations of the amplitude of the electric field above the integrated structure. As expected, SPP are only excited with the TM mode.

mode [17,40]. Also, the mode is laterally confined in the IExWg region with FWHM $= 0.62 \pm 0.11$ μm.

To corroborate the experimental results, we calculated the electric field distribution along the gold nanoslab on IExWg with the use of a 3D finite difference time domain method implemented by Lumerical. We imported the refractive index of the IExWg into Lumerical following the indications in the manual (import of nk files) and placed the gold nanoslab on top of the waveguide with a dielectric permittivity for gold measured in our lab by spectral ellipsometry. The electric field distributions measured 20 nm above the surface of the structure complement the experimental results. The TE photonic mode of the IExWg does not excite the SPP [Fig. 6(e)], while the TM mode efficiently excites the hybrid mode of the integrated structure [Fig. 6(f)]. The intensity map of Figure 6(f) show that the intensity decays when light propagates through the nanoslab, which is a natural result due to optical absorption in metals. As we used the NSOM technique in the transmission configuration, this propagation loss is not observed in Fig. 6(d) because

this technique registers the variations of the intensity of light transmitted at the output of the IExWg when the AFM probe scans the measured area [45–47]. However, these experimental results (Figs. 6d and 6f) confirm the mode beating that arises from the predicted mode hybridization.

4. CONCLUSIONS

By using theoretical diffusion modeling, we designed and modeled the optical properties of an ion-exchanged waveguide in a glass substrate to analyze the distribution of its refractive index and effective refractive index of the supported modes. Specifically, for a diffusion window of 1.5 μm, the IExWg supported two nondegenerated orthogonal photonic modes in the visible and near-infrared region of the electromagnetic spectrum. Also, using numerical simulations, we predicted that the SPP of a metallic layer would be efficiently excited with the photonic mode of an IExWg as the phase-matching condition for these resonances was satisfied.

Then, by using the NSOM technique, we characterized a simplistic integrated device consisting of a gold nanoslab placed on top of an IExWg. As theoretically predicted, the SPP supported by the metallic structure was efficiently excited with the photonic mode of the waveguide. We also corroborated that, due to the geometry of the structure, the hybrid photonic–plasmonic mode of the integrated structure was only excited with the fundamental TM mode of the waveguide. This result also implies that the photonic modes of the IExWg are nondegenerated and that the polarization is preserved along the propagation length. In general, we demonstrated the feasibility of using IExWg for the development of integrated metaphotonic devices. Further investigation could be performed to improve the coupling efficiency between IExWg and SPP modes. Besides their low-cost fabrication, low propagation losses, low birefringence (to prevent nonlinear effects or spatial mode distortion) and high compatibility with commercial optical fibers, glass waveguide technology has the advantage of operating at visible wavelengths. For instance, this property can be used in single molecule detection or biosensing by measuring either the spectral shift at the output of the IExWg caused by antigen–antibody functionalization, or by measuring luminescence with conventional spectral microscopy systems. Due to their material compatibility with commercial optical fibers, these hybrid systems also can be employed for signal filtering, opening new perspectives in the design of optical circuits.

Funding. Consejo Nacional de Ciencia y Tecnología (296355, 50719, 692214).

Acknowledgment. The authors thank CONACYT for partial financial support. Computations were carried out with the resources of the French regional Grand-Est HPC Center ROMEO. The fabrication was done at the French Regional Grand Est nanofabrication and nanocharacterization platform (Nano'Mat).

Disclosures. The authors declare no conflicts of interest.

REFERENCES

1. A. Baev, P. N. Prasad, H. Ågren, M. Samoć, and M. Wegener, "Metaphotonics: an emerging field with opportunities and challenges," Phys. Rep. **594**, 1–60 (2015).
2. N. Engheta, B. Edwards, I. Liberal, N. M. Estakhri, A. Mahmoud, and Y. Lumer, "Extreme platforms for metaphotonics," in *Conference on Lasers and Electro-Optics (CLEO)* (2017), pp. 1–2.
3. K. Liu, S. Sun, A. Majumdar, and V. J. Sorger, "Fundamental scaling laws in nanophotonics," Sci. Rep. **6**, 37419 (2016).
4. B. Wang, S. Blaize, J. Seok, S. Kim, H. Yang, and R. Salas-Montiel, "Plasmonic-based subwavelength graphene-on-hBN modulator on silicon photonics," IEEE J. Sel. Top. Quantum Electron. **25**, 4600706 (2019).
5. P. Cheben, R. Halir, J. H. Schmid, H. A. Atwater, and D. R. Smith, "Subwavelength integrated photonics," Nature **560**, 565–572 (2018).
6. J. Wang, S. Paesani, Y. Ding, R. Santagati, P. Skrzypczyk, A. Salavrakos, J. Tura, R. Augusiak, L. Mančinska, D. Bacco, D. Bonneau, J. W. Silverstone, Q. Gong, A. Acín, K. Rottwitt, L. K. Oxenløwe, J. L. O'Brien, A. Laing, and M. G. Thompson, "Multidimensional quantum entanglement with large-scale integrated optics," Science **360**, 285–291 (2018).
7. A. H. Atabaki, S. Moazeni, F. Pavanello, H. Gevorgyan, J. Notaros, L. Alloatti, M. T. Wade, C. Sun, S. A. Kruger, H. Meng, K. Al Qubaisi, I. Wang, B. Zhang, A. Khilo, C. V. Baiocco, M. A. Popović, V. M. Stojanović, and R. J. Ram, "Integrating photonics with silicon nanoelectronics for the next generation of systems on a chip," Nature **556**, 349–354 (2018).
8. Y. Shen, N. C. Harris, S. Skirlo, M. Prabhu, T. Baehr-Jones, M. Hochberg, X. Sun, S. Zhao, H. Larochelle, D. Englund, and M. Soljačić, "Deep learning with coherent nanophotonic circuits," Nat. Photonics **11**, 441 (2017).
9. R. Tellez-Limon, B. Bahari, L. Hsu, J.-H. Park, A. Kodigala, and B. Kanté, "Integrated metaphotonics: symmetries and confined excitation of LSP resonances in a single metallic nanoparticle," Opt. Express **24**, 13875–13880 (2016).
10. N. Kinsey, M. Ferrera, V. M. Shalaev, and A. Boltasseva, "Examining nanophotonics for integrated hybrid systems: a review of plasmonic interconnects and modulators using traditional and alternative materials [invited]," J. Opt. Soc. Am. B **32**, 121–142 (2015).
11. W. Yan and N. A. Mortensen, "Nonclassical effects in plasmonics: an energy perspective to quantify nonclassical effects," Phys. Rev. B **93**, 115439 (2016).
12. Q. Liu, J. S. Kee, and M. K. Park, "Grating-assisted excitation of short-range surface plasmon polariton mode," IEEE Photon. Technol. Lett. **25**, 1420–1423 (2013).
13. Q. Liu and K. S. Chiang, "Planar long-period grating filter based on long-range surface plasmon mode of buried metal stripe waveguide," Opt. Express **18**, 8963–8968 (2010).
14. R. Quidant, C. Girard, J.-C. Weeber, and A. Dereux, "Tailoring the transmittance of integrated optical waveguides with short metallic nanoparticle chains," Phys. Rev. B **69**, 085407 (2004).
15. F. Bernal Arango, A. Kwadrin, and A. F. Koenderink, "Plasmonic antennas hybridized with dielectric waveguides," ACS Nano **6**, 10156–10167 (2012).
16. M. Février, P. Gogol, A. Aassime, R. Mégy, C. Delacour, A. Chelnokov, A. Apuzzo, S. Blaize, J.-M. Lourtioz, and B. Dagens, "Giant coupling effect between metal nanoparticle chain and optical waveguide," Nano Lett. **12**, 1032–1037 (2012).
17. R. Tellez-Limon, M. Février, A. Apuzzo, R. Salas-Montiel, and S. Blaize, "Numerical analysis of tip-localized surface plasmon resonances in periodic arrays of gold nanowires with triangular cross section," J. Opt. Soc. Am. B **34**, 2147–2154 (2017).
18. R. Bruck and O. L. Muskens, "Plasmonic nanoantennas as integrated coherent perfect absorbers on SOI waveguides for modulators and all-optical switches," Opt. Express **21**, 27652–27661 (2013).
19. M. Chamanzar and A. Adibi, "Hybrid nanoplasmonic-photonic resonators for efficient coupling of light to single plasmonic nanoresonators," Opt. Express **19**, 22292–22304 (2011).
20. M. Chamanzar, Z. Xia, S. Yegnanarayanan, and A. Adibi, "Hybrid integrated plasmonic-photonic waveguides for on-chip localized surface

plasmon resonance (LSPR) sensing and spectroscopy," Opt. Express **21**, 32086–32098 (2013).
21. A. A. Meza-Olivo, K. Garay-Palmett, S. Blaize, and R. Salas-Montiel, "Reciprocity and Babinet's principles applied to the enhancement of the electric and magnetic local density of states in integrated plasmonics on silicon photonics," Appl. Opt. **57**, 9155–9163 (2018).
22. A. Espinosa-Soria, E. Pinilla-Cienfuegos, F. J. Díaz-Fernández, A. Griol, J. Martí, and A. Martínez, "Coherent control of a plasmonic nanoantenna integrated on a silicon chip," ACS Photon. **5**, 2712–2717 (2018).
23. M.-F. Tsai, S.-H. G. Chang, F.-Y. Cheng, V. Shanmugam, Y.-S. Cheng, C.-H. Su, and C.-S. Yeh, "Au nanorod design as light-absorber in the first and second biological near-infrared windows for in vivo photothermal therapy," ACS Nano **7**, 5330–5342 (2013).
24. I. Krasnokutska, R. J. Chapman, J.-L. J. Tambasco, and A. Peruzzo, "High coupling efficiency grating couplers on lithium niobate on insulator," Opt. Express **27**, 17681–17685 (2019).
25. C. Bellegarde, H. E. Dirani, X. Letartre, C. Petit-Etienne, C. Monat, J.-M. Hartmann, C. Sciancalepore, and E. Pargon, "Technological advances on Si and Si3N4 low-loss waveguide platforms for nonlinear and quantum optics applications," Proc. SPIE **10933**, 16–23 (2019).
26. M. Ma, A. H. K. Park, Y. Wang, H. Shoman, F. Zhang, N. A. F. Jaeger, and L. Chrostowski, "Sub-wavelength grating-assisted polarization splitter-rotators for silicon-on-insulator platforms," Opt. Express **27**, 17581–17591 (2019).
27. T. Izawa and H. Nakagome, "Optical waveguide formed by electrically induced migration of ions in glass plates," Appl. Phys. Lett. **21**, 584–586 (1972).
28. R. Terai and R. Hayami, "Ionic diffusion in glasses," J. Non-Cryst. Solids **18**, 217–264 (1975).
29. T. Findakly, "Glass waveguides by ion exchange: a review," Opt. Eng. **24**, 242244 (1985).
30. R. V. Ramaswamy and R. Srivastava, "Ion-exchanged glass waveguides: a review," J. Lightwave Technol. **6**, 984–1000 (1988).
31. A. Tervonen, S. K. Honkanen, and B. R. West, "Ion-exchanged glass waveguide technology: a review," Opt. Eng. **50**, 071107 (2011).
32. L. Arnaud, A. Bruyant, M. Renault, Y. Hadjar, R. Salas-Montiel, A. Apuzzo, G. Lérondel, A. Morand, P. Benech, E. L. Coarer, and S. Blaize, "Waveguide-coupled nanowire as an optical antenna," J. Opt. Soc. Am. A **30**, 2347–2355 (2013).
33. J. B. Madrigal, R. Tellez-Limon, F. Gardillou, D. Barbier, W. Geng, C. Couteau, R. Salas-Montiel, and S. Blaize, "Hybrid integrated optical waveguides in glass for enhanced visible photoluminescence of nanoemitters," Appl. Opt. **55**, 10263–10268 (2016).
34. J.-E. Broquin, "Glass integrated optics: state of the art and position toward other technologies," Proc. SPIE **6475**, 647507 (2007).
35. J.-E. Broquin, "Ion-exchanged integrated devices," Proc. SPIE **4277**, 105–117 (2001).
36. P. Y. Choo, J. A. Frantz, J. Carriere, D. L. Mathine, R. K. Kostuk, and N. Peyghambarian, "Measurement and modeling of ion-exchange parameters for IOG-10 glass," Opt. Eng. **42**, 2812–2816 (2003).
37. S. A. Maier, *Plasmonics: Fundamentals and Applications* (Springer, 2007).
38. E. Devaux, T. W. Ebbesen, J.-C. Weeber, and A. Dereux, "Launching and decoupling surface plasmons via micro-gratings," Appl. Phys. Lett. **83**, 4936–4938 (2003).
39. B. Hecht, H. Bielefeldt, L. Novotny, Y. Inouye, and D. W. Pohl, "Local excitation, scattering, and interference of surface plasmons," Phys. Rev. Lett. **77**, 1889–1892 (1996).
40. R. Tellez-Limon, M. Fevrier, A. Apuzzo, R. Salas-Montiel, and S. Blaize, "Theoretical analysis of Bloch mode propagation in an integrated chain of gold nanowires," Photon. Res. **2**, 24–30 (2014).
41. A. Yariv, "Coupled-mode theory for guided-wave optics," IEEE J. Quantum Electron. **9**, 919–933 (1973).
42. H. A. Haus and W. Huang, "Coupled-mode theory," Proc. IEEE **79**, 1505–1518 (1991).
43. C. Chen, X. Xu, A. Hosseini, Z. Pan, H. Subbaraman, X. Zhang, and R. T. Chen, "Design of highly efficient hybrid Si-Au taper for dielectric strip waveguide to plasmonic slot waveguide mode converter," J. Lightwave Technol. **33**, 535–540 (2015).
44. S. Aubert, A. Bruyant, S. Blaize, R. Bachelot, G. Lerondel, S. Hudlet, and P. Royer, "Analysis of the interferometric effect of the background light in apertureless scanning near-field optical microscopy," J. Opt. Soc. Am. B **20**, 2117–2124 (2003).
45. J. T. Robinson, S. F. Preble, and M. Lipson, "Imaging highly confined modes in sub-micron scale silicon waveguides using transmission-based near-field scanning optical microscopy," Opt. Express **14**, 10588–10595 (2006).
46. R. Salas-Montiel, A. Apuzzo, A. Bruyant, P. Royer, G. Lérondel, and S. Blaize, "Optical near field in silicon photonics," Proc. SPIE **7943**, 187–198 (2011).
47. R. Salas-Montiel, A. Apuzzo, C. Delacour, Z. Sedaghat, A. Bruyant, P. Grosse, A. Chelnokov, G. Lerondel, and S. Blaize, "Quantitative analysis and near-field observation of strong coupling between plasmonic nanogap and silicon waveguides," Appl. Phys. Lett. **100**, 231109 (2012).